J. Fluid Mech. (2016), *vol.* 798, *pp.* 371–397. © Cambridge University Press 2016
doi:10.1017/jfm.2016.319

Three-dimensional instabilities in oscillatory flow past elliptic cylinders

José P. Gallardo[1,†], Helge I. Andersson[2] and Bjørnar Pettersen[1]

[1]Department of Marine Technology, Norwegian University of Science and Technology, NO-7491 Trondheim, Norway

[2]Department of Energy and Process Engineering, Norwegian University of Science and Technology, NO-7491 Trondheim, Norway

(Received 10 February 2015; revised 16 February 2016; accepted 4 May 2016; first published online 3 June 2016)

We investigate the early development of instabilities in the oscillatory viscous flow past cylinders with elliptic cross-sections using three-dimensional direct numerical simulations. This is a classical hydrodynamic problem for circular cylinders, but other configurations have received only marginal attention. Computed results for some different aspect ratios Λ from 1 : 1 to 1 : 3, all with the major axis of the ellipse aligned in the main flow direction, show good qualitative agreement with Hall's stability theory (*J. Fluid Mech.*, vol. 146, 1984, pp. 347–367), which predicts a cusp-shaped curve for the onset of the primary instability. The three-dimensional flow structures for aspect ratios larger than 2 : 3 resemble those of a circular cylinder, whereas the elliptical cross-section with the lowest aspect ratio of 1 : 3 exhibits oblate rather than tubular three-dimensional flow structures as well as a pair of counter-rotating spanwise vortices which emerges near the tips of the ellipse. Contrary to a circular cylinder, instabilities for an elliptic cylinder with sufficiently high eccentricity emerge from four rather than two different locations in accordance with the Hall theory.

Key words: separated flows, vortex dynamics, vortex instability

1. Introduction

1.1. *Oscillatory viscous flows*

A canonical problem in marine hydrodynamics is that of the oscillatory flow around a cylindrical body. In its simplest form, which is used as a prototype to study more complex cases, the flow is considered to be sinusoidal, unidirectional and perpendicular to the axis of a circular cylinder. This periodic motion is characterized by the Keulegan–Carpenter number $KC = U_m T/D$ (Keulegan & Carpenter 1958), where U_m is the velocity amplitude, T is the period of the motion and D is the diameter of the circular cylinder. Viscous effects are taken into account by a second governing parameter: the Reynolds number $Re = U_m D/\nu$, with ν the

† Email address for correspondence: jose.p.gallardo@ntnu.no

kinematic viscosity. Additionally, the Stokes number $\beta = Re/KC = D^2/T\nu$ (Sarpkaya 2005) is used by convention in combination with KC to map the different flow regimes. A rich set of flow patterns is obtained by varying KC and β; for the simplest cylindrical geometry, the circular cylinder, they have been well documented by e.g. Tatsuno & Bearman (1990) and Elston, Blackburn & Sheridan (2006).

For low values of KC and β the unsteady flow remains attached to the cylinder, and is completely symmetrical and two-dimensional, with a reflection symmetry about the axis of oscillation. As the governing parameters are gradually increased a first three-dimensional instability appears (Honji 1981), but a spatio-temporal symmetry is retained in the plane normal to the axis of the cylinder. Vortex shedding and separation are characteristics of the regimes at high KC; Williamson (1985) associated the different shedding regimes with a certain KC range and Bearman *et al.* (1985) studied the contribution from vortex shedding and separation to the in-line forces.

1.2. *Primary and secondary instabilities*

Contrary to the steady flow past a circular cylinder, whose primary instability is two-dimensional, the primary instability of the oscillating flow past a circular cylinder is three-dimensional. Previous investigators have claimed this to be a centrifugal instability induced by the curvature of the cylinder (Honji 1981; Hall 1984). Observations of the streaked flow by Honji were validated by instability analysis of Hall (1984), who found a critical line in the (KC, β)-plane for this instability, in very good agreement with Honji's experimental results. The mushroom-shaped structures were also visualized in experiments by Sarpkaya (1986), who extended the study of this primary instability using several high-speed video cameras and laser-induced fluorescence (Sarpkaya 2002). This last study resulted in a classification of the region around the instability line into four different states: stable, marginal, unstable and chaotic. Numerical simulations have contributed considerably to the knowledge about the Honji instability by means of detailed visualizations of the structure of the Honji vortices, and explanations of the dynamics involved in their formation (see e.g. Zhang & Dalton 1999; An, Cheng & Zhao 2011; Suthon & Dalton 2011, 2012).

As the oscillation amplitude U_m increases further, vortices are formed and shed during each half-cycle. This results in secondary instabilities that break the symmetry in the plane normal to the cylinder axis, producing a set of fascinating flow patterns. Eight different regimes were visualized and grouped according to their characteristics by Tatsuno & Bearman (1990) at $1.6 \leqslant KC \leqslant 15$ and $5 \leqslant \beta \leqslant 160$. This classification was extended by Elston *et al.* (2006), who used Floquet analysis and direct numerical simulations to map the symmetry-breaking instabilities in the (KC, β)-plane at $KC \leqslant 10$ and $\beta \leqslant 100$. Depending on the Stokes number, two different manifestations of the secondary instability were observed in their study: at low Stokes numbers the instability was synchronous with the imposed oscillation, resulting in a characteristic boomerang-shaped mode, whereas higher Stokes numbers resulted in a quasi-periodic instability with a clear second period.

1.3. *Instability theory for elliptic cylinders*

Hall (1984) extended his instability theory for circular cylinders to more general geometries; in particular, cylinders with an elliptic cross-section. He showed that for certain orientations of an elliptic cylinder the locations at which the instability arises depend on the aspect ratio of the cylinder, i.e. the ratio between the minor and major

axis $\Lambda = b/a$. Throughout the present paper we adopt the parametric representation of the ellipse,

$$x = \frac{a}{2}\cos\phi \quad \text{and} \quad y = \frac{b}{2}\sin\phi, \tag{1.1a,b}$$

with $0 \leqslant \phi \leqslant 2\pi$. The most stable configuration is that with the major axis aligned with the oscillatory flow direction, in which case the orientation angle α is zero.

For a circular cylinder ($\Lambda = 1$) the instability is located at an angle $\phi_1 = \pi/2$ from the stagnation points (i.e. at the shoulders of the cylinder), which is the region where the flow reaches maximum acceleration. According to Hall, for an elliptic cylinder with $\alpha = 0$ the location of the instability remains at the shoulders of the cylinder for Λ larger than a critical value $\sqrt{3/5}$. As Λ decreases below this critical value the location of the instability is displaced towards the stagnation points. In this case six critical points arise on the ellipse: two at $\pm\pi/2$ from the stagnation points, and four at a critical angle ϕ_m symmetrically located with respect to the minor and major axes. As pointed out by Hall (1984), this shift in the critical points is due to the increasing eccentricity of the ellipse as the aspect ratio Λ decreases. From the stability analysis he showed that the flow is neutrally stable at an angle ϕ_m by considering the maxima of the function

$$S(\phi) = \sin^2(\phi - \alpha)(\sin^2\phi + \Lambda^2\cos^2\phi)^{-5/2}. \tag{1.2}$$

When, for instance, $\alpha = 0$ and $\Lambda < \sqrt{3/5}$ two additional critical points appear at

$$\phi = \phi_2 = \sin^{-1}\left(\frac{2\Lambda^2}{3(1-\Lambda^2)}\right)^{1/2} \quad \text{and} \quad \phi = \phi_3 = \pi - \phi_2, \tag{1.3a,b}$$

and the instability curve depicted in figure 1(*b*) bifurcates into two branches for aspect ratios Λ below the critical aspect ratio $\sqrt{3/5}$. For lower aspect ratios the angle ϕ_m departs from the standard value $\pi/2$ for circular cylinders.

Whether the oscillating flow is stable or unstable is determined by the local Taylor number

$$Ta_\ell = \frac{2}{\pi^{3/2}}\beta^{1/2}KC^2\frac{\Lambda^{1/2}(1+\Lambda)^2\sin^2\phi}{(\sin^2\phi + \Lambda^2\cos^2\phi)^{5/2}}, \tag{1.4}$$

which represents a measure of the ratio between centrifugal and viscous forces. Hall's (1984) linear stability analysis demonstrated that the flow is neutrally stable when $Ta_\ell = 11.99$ at $\phi = \phi_m$ and accordingly unstable for higher values of Ta_ℓ. For the sake of convenience, Hall also introduced the global or non-local Taylor number

$$Ta = \frac{2}{\pi^{3/2}}\beta^{1/2}KC^2\Lambda^{-1/2}. \tag{1.5}$$

Hall's instability diagram for the particular orientation $\alpha = 0°$ of the elliptic cylinder has been reproduced in figure 1(*a*) in which the curves for neutral instability are shown. Here, $Ta_0 = 11.99/4 \approx 3.0$ is the critical value of the global Taylor number Ta for $\Lambda = 1$, i.e. for a circular cylinder.

Apart from Hall's analysis, there are not many studies involving oscillating flows past an elliptic cylinder. Badr & Kocabiyik (1997) investigated the oscillating viscous flow around an elliptic cylinder by integrating the vorticity-transport

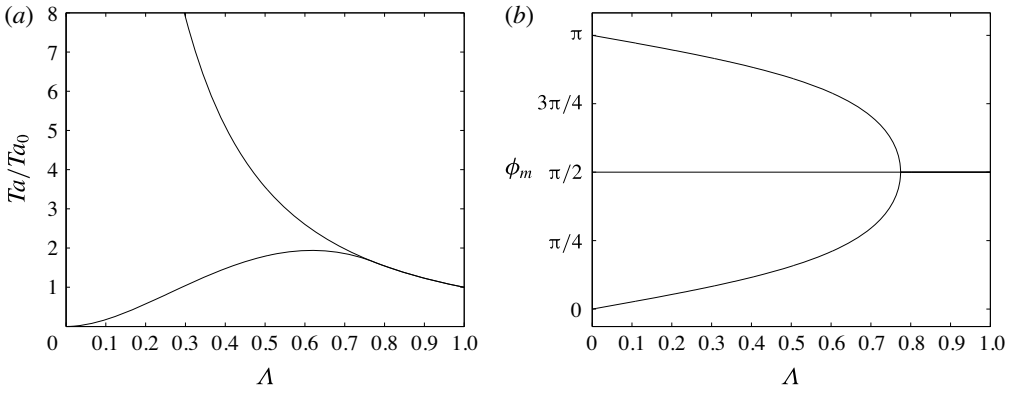

FIGURE 1. Instability curves reproduced in accordance with Hall's (1984) analysis for an orientation angle $\alpha = 0°$. (*a*) Cusp-shaped curve depicting the dependence of the critical Taylor number Ta/Ta_0 on Λ; and (*b*) dependence of the critical angle ϕ_m on Λ. The critical case corresponds to $\Lambda = \sqrt{3/5} \approx 0.775$ and the lowest-eccentricity case is for $\Lambda = 1.0$ (circular cylinder).

equation in combination with the stream function equation. However, their study was two-dimensional and with focus on separated flow. In the course of the final revision of this paper, we incidentally became aware of another computational study of oscillatory flow around a cylinder with an elliptic cross-section by Yang (2014). The three-dimensional Navier–Stokes equations were integrated numerically with the same finite-element method as that already used by An *et al.* (2011) and Yang *et al.* (2014) with the view to explore the effects of the elliptic cross-sections.

1.4. *Objectives and approach*

Although the oscillating flow problem has been extensively studied for circular cylinders, little is known about the different regimes and instabilities resulting from the oscillating flow past an elliptic cylinder. One may intuitively anticipate that the unsteady flow field in the vicinity of an elliptic cylinder crucially depends on its eccentricity and only resembles that around a circular cylinder when $\Lambda \approx 1$. This problem has practical importance for some applications such as piles, submarine sections and wings. The main challenge in this case is the presence of two additional parameters: the aspect ratio Λ and the orientation α of the ellipse relative to the flow direction. In the present study we investigate, for the first time to the authors' knowledge, the primary three-dimensional instability for a cylinder with an elliptic cross-section oriented with its major axis parallel to the main flow direction ($\alpha = 0°$); this orientation, according to Hall's analysis, exhibits a cusp-shaped instability curve. Four representative aspect ratios are chosen for this purpose. In order to obtain sufficient details of the flow dynamics and the three-dimensional structure of the primary instability, our approach is to solve directly the full three-dimensional Navier–Stokes equations. Although the main focus here is on the primary instability predicted by Hall (1984), also known as the Honji instability, we also present results of the transition towards the secondary instability that motivate future work.

This paper is arranged in the following way. First, in § 2 we define the problem according to the governing parameters discussed above, and describe the flow configuration used for the simulations. Next, in § 3 we present details concerning

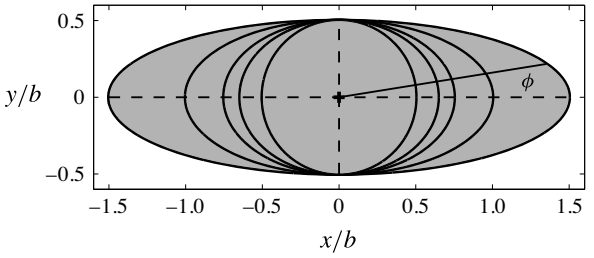

FIGURE 2. Sketch of the different cylindrical configurations considered in the present study. The orientation angle is $\alpha = 0°$, which corresponds to the most stable configuration according to Hall (1984). Here the selected ratios between the minor and major axis $\Lambda = b/a$ are $1/3$, $1/2$, $2/3$, $\sqrt{3/5}$; the circular cylinder with $\Lambda = 1$ is also included as reference. An important parameter used throughout the present study is the angle ϕ, which is measured anticlockwise from the stagnation point $(a/2, 0)$.

the numerical methodology and the grid studies. The presentation of results starts with a preliminary exploration of the effects of ellipticity in § 4, where we compare the vortical structures for different Λ at the same phase. This is followed by a detailed analysis of the evolution of the flow structures for the case with highest ellipticity ($\Lambda = 1/3$) in § 5. In this particular cylinder case we consider five different values of the parameter β for fixed KC. Finally, a summary and concluding remarks are given in § 6.

2. Problem definition and methodology

2.1. *Governing parameters*

Hall's instability theory for an elliptic cylinder is valid for any orientation α and aspect ratio Λ. Due to the high computational cost of directly solving the three-dimensional Navier–Stokes equations, we have chosen to study only flow configurations with orientation $\alpha = 0°$ (i.e. with the major axis of the ellipse aligned with the oscillatory flow), and aspect ratios $\Lambda = 1/3$, $1/2$, $2/3$ and $\sqrt{3/5}$ (see figure 2).

According to Hall's theory $\alpha = 0°$ is the most stable configuration and exhibits a cusp-shaped instability curve, thereby providing the opportunity to observe three-dimensional instabilities for Taylor numbers above the lower branch of this cusp-shaped curve in figure 1(*a*). For carefully selected combinations of the governing parameters KC and β, we expect to observe vortices similar to those observed by Honji (1981) in his experiments with an oscillating circular cylinder. Given the direction of the oscillating flow, the Reynolds number Re is defined using the transverse scale b, whereas the Keulegan–Carpenter number KC is defined with the major axis a as the length scale,

$$KC = \frac{U_m T}{a}, \quad Re = \frac{U_m b}{\nu}, \quad \beta = \frac{Re}{KC} = \frac{ab}{\nu T}. \tag{2.1a–c}$$

Thus, with basis in Hall's theory, several combinations of KC and β were considered for the simulations, and the cases with clear three-dimensional instabilities were selected for further examination throughout this paper. Table 1 presents a summary of the main parameters for these cases. In table 1 we also include an estimate for the

Case	Λ	KC	β	Re	Ta	λ_z/b	λ'_z/b
C_{1a}		2.0	200	400	35.19	—	—
C_{1b}		2.0	300	600	43.10	1.00	0.70
C_{1c}	1/3	2.0	400	800	49.77	1.00	0.60
C_{1d}		2.0	500	1000	55.64	$\approx$1.00	0.54
C_{1e}		2.0	600	1200	60.95	$\approx$1.00	0.49
C_2	1/2	2.0	300	600	35.19	0.80–1.00	0.57
C_3	2/3	2.0	200	400	24.88	0.80	0.60
C_4	$\sqrt{3/5}$	2.0	200	400	23.09	0.80	0.56
C_5	1	2.0	200	400	20.32	0.67	0.49

TABLE 1. Summary of the cases exhibiting three-dimensional instabilities considered in the present study. Here KC is the Keulegan–Carpenter number, β the Stokes number, Re the Reynolds number, Ta the global Taylor number, λ_z the axial wavelength of the three-dimensional instability obtained from the simulations and λ'_z the theoretical estimate (2.3) for this axial wavelength. Note that the critical value of the global Taylor number for a circular cross-section is $Ta_0 = 11.99/4 \approx 3.0$.

axial wavelength of the three-dimensional instability λ'_z. This theoretical prediction is obtained from the scaling in Hall's equations (2.1b) and (1.1a), together with his critical wavenumber $k_c = 0.51$ (Hall's equation (3.1b)),

$$\lambda'_z = \frac{2\pi}{k_c}\left(\frac{\nu T}{\pi}\right)^{1/2}. \tag{2.2}$$

Using the Stokes number β as defined in (2.1) we obtain

$$\lambda'_z = \frac{2\pi}{k_c}(\pi\Lambda\beta)^{-1/2}b. \tag{2.3}$$

According to expression (2.3), λ'_z decreases as Λ and β increase. Although the predicted values λ'_z in table 1 are always lower than those obtained from the numerical simulations, predicted and observed axial wavelengths have the same order of magnitude.

2.2. *Governing equations*

The governing equations are the incompressible Navier–Stokes equations for a fluid with constant density ρ and kinematic viscosity ν, which expressed in non-dimensional form are

$$\frac{\partial u_i}{\partial x_i} = 0, \tag{2.4}$$

$$\frac{1}{KC}\frac{\partial u_i}{\partial t} + u_j\frac{\partial u_i}{\partial x_j} = -\frac{\partial p}{\partial x_i} + \frac{1}{Re}\frac{\partial^2 u_i}{\partial x_j \partial x_j}. \tag{2.5}$$

The flow field is determined by the velocity u_i in each of the three Cartesian directions x_i, with $i = 1, 2, 3$, and the pressure p. In the present context u, v, w refer to the streamwise, cross-stream and spanwise velocity components, respectively, and t is non-dimensional time normalized with T.

3. Numerical aspects

3.1. *Numerical solution of the governing equations*

The flow field is computed numerically by directly solving the governing momentum equation (2.5) subject to the incompressibility constraint (2.4). To accomplish this, we use the Navier–Stokes solver MGLET (Manhart, Tremblay & Friedrich 2001; Manhart 2004). This is a finite-volume code with second-order spatial accuracy in which the flow variables are defined on a staggered Cartesian grid. Good convergence properties are achieved in the numerical solution of the Poisson equation for pressure correction by using the strongly implicit procedure (SIP) by Stone (1968), accelerated with a multigrid algorithm. For the time integration we use an explicit low-storage third-order Runge–Kutta scheme (Williamson 1980).

To represent the elliptic cylinders inside the computational domain, we use an immersed boundary (IB) method based on direct forcing to specify the no-slip and impermeability boundary conditions at the cylinder surface. In order to ensure mass conservation a flux correction based on the cell volumes at the fluid–solid interface is applied. The description of this IB method and its validation can be found in Peller *et al.* (2006).

The computational domain is defined as a box in which the cylinder axis coincides with the origin in the (x, y)-plane. In the (x, y)-plane the computational box spans $50b \times 50b$. This size was chosen based on previous experience with oscillatory flow around a circular cylinder, and domain sizes used by previous authors for similar flows (see e.g. Elston *et al.* 2006; An *et al.* 2011). With the exception of cases C_{1d} and C_{1e}, vortices are not shed from the cylinder, and when shedding occurs they never reach the boundaries of the domain. Depending on the spanwise wavelength λ_z of the primary instability two different spanwise-domain lengths L_z of $4b$ and $8b$ were considered.

Concerning numerical boundary conditions, we use the following:

(i) Oscillating velocity $[u, 0, 0] = U_m[\cos(2\pi t/T), 0, 0]$, with U_m the maximum velocity amplitude at the (y, z)-plane $x/b = -25$.

(ii) At the (y, z)-plane at $x/b = 25$ a Neumann boundary condition is imposed for the velocities $(\partial u/\partial x = \partial v/\partial x = \partial w/\partial x = 0)$, and the pressure is set to zero $(p = 0)$.

(iii) Periodicity is prescribed at the top and bottom (x, y)-planes to mimic an infinitely long cylinder.

(iv) At the remaining side (x, z)-planes we prescribe a free-slip boundary condition. This corresponds to $v = 0$ and $\partial u/\partial y = \partial w/\partial y = 0$ at $y/b = \pm 25$.

3.2. *Grid refinement tests*

Grid tests were conducted for the cases with $\Lambda = 1/3$ because, as mentioned above, these cases exhibit the largest Re. The main quantities considered to study the different grid resolutions were the in-line force coefficients, and the growth of the instabilities based on the spanwise velocity w. Force coefficients were obtained by decomposing the drag and inertia forces according to Morison's equation (Morison *et al.* 1950). Since the KC numbers considered in this study are relatively low, the inertia force dominates over the drag force in all the cases considered. Three different grid resolutions for case C_{1c} were examined (see table 2). In all the simulations the time step Δt was set to one-tenth of Δ_{min}/U_m, with Δ_{min} the minimum grid spacing, in order to ensure low divergence and numerical stability.

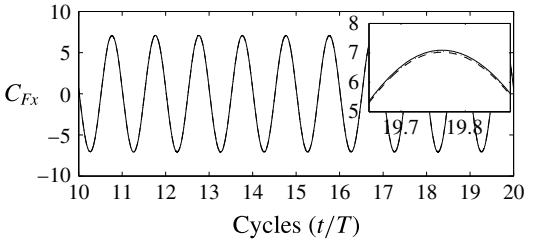

FIGURE 3. The time evolution of the in-line force coefficient $C_{Fx} = F_x/0.5\rho U_m^2 L_z b$ for three different grid resolutions at $\Lambda = 1/3$ (C_{1c}): fine (——), medium (- - -) and coarse ($\cdots\cdots$) grids. The inset plot zooms into the peaks of the force coefficients, depicting minute differences for different grid resolutions.

Case	Grid	Δ_{min}/b	$N_x \times N_y \times N_z$	C_d	C_m	Growth rate
	Coarse	0.010	$544 \times 352 \times 64$	0.7303	1.4248	0.0009
C_{1c}	Medium	0.0075	$674 \times 400 \times 64$	0.7238	1.4231	0.0140
	Fine	0.005	$896 \times 512 \times 64$	0.7256	1.4298	0.0123

TABLE 2. The drag and inertia coefficients, C_d and C_m respectively, and linear growth rates for $\Lambda = 1/3$ and $Re = 800$ for different grid resolutions.

Table 1 shows that the wavelength λ_z/b for case C_{1c} is 1.0, and hence a grid spacing in the spanwise direction $\Delta_z/b = 0.0625$ was sufficient to resolve the three-dimensional flow structures.

Since the excursions from $Re = 800$ are relatively low for C_{1d} and C_{1e}, these cases were simulated with the same grid resolutions in the x- and y-directions as for case C_{1c}. All the cases with $\Lambda = 1/3$ were simulated using a spanwise length $L_z/b = 8$. The wavelength of the three-dimensional instability for cases C_{1b} and C_{1c} is comparatively large, therefore a spanwise length of $L_z/b = 8$ was considered sufficient. However, no differences in the flow properties were observed for this case with a shorter spanwise length.

Table 2 shows that the force coefficients C_d and C_m exhibit only a modest dependence on the grid refinement, with differences only in the third significant digit. The non-monotonic trend from the coarse to fine grids for case C_{1c} can be explained by the fact that the three-dimensional instabilities are not triggered in the coarse grid. Figure 3 shows the time evolution of the in-line force coefficients for case C_{1c} with different grid resolutions. Even in the inset plot zooming into the peaks the differences are barely distinguishable for the different resolutions considered.

When studying the primary three-dimensional instability, an important factor in deciding an adequate grid resolution is the development of the instability in time. This issue was examined for case C_{1c} in figure 4, where the time history of the spanwise velocity w is shown for different grid resolutions. This velocity component was sampled at regularly spaced points along a line parallel to the cylinder axis, located at $\phi = 48°$ from the stagnation point $(-a/2, 0)$, and at a distance of $0.15b$ from the cylinder surface. No artificial perturbations were added to trigger the instability. It is evident from figure 4 that the growth of this velocity component converges to a rate of the order of 0.01 with sufficient grid resolution (see also table 2). Even more

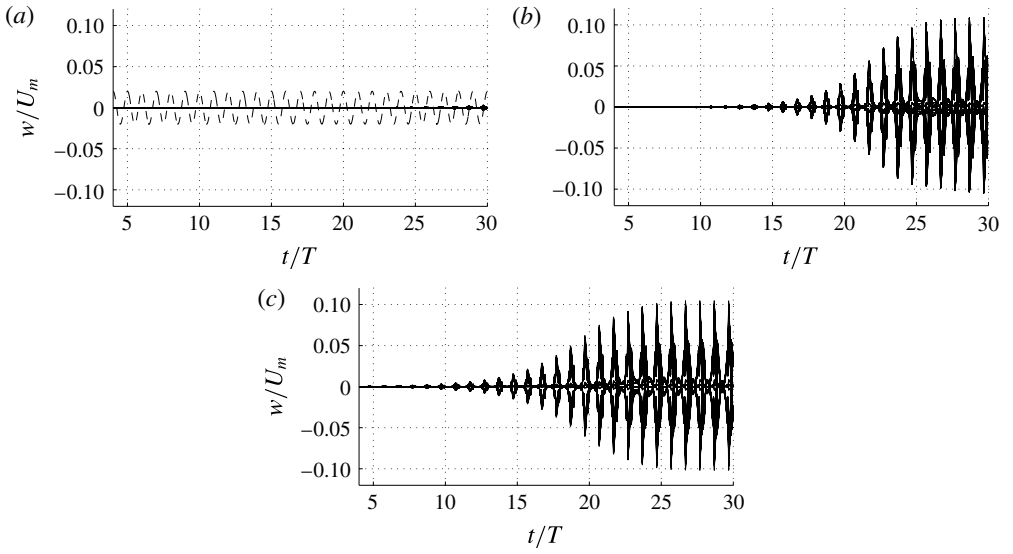

FIGURE 4. Time history of the spanwise velocity w depicting the growth of the three-dimensional instability for different grid resolutions. Case considered is C_{1c} with $\Lambda = 1/3$, $KC = 2$ and $\beta = 400$; (*a*) coarse, (*b*) medium and (*c*) fine grid resolutions. The dashed curve in (*a*) reflects the time variation of the free-stream velocity.

striking is the almost total absence of three-dimensional instabilities after 30 cycles using a coarse grid resolution (figure 4*a*). We recall that in this case the refinement is in the (x, y)-plane only.

The growth rate is introduced as a measure of how fast the instability grows until regular oscillations with almost constant amplitude have been established. The actual growth rate reported in table 2 is non-dimensionalized using T and estimated from the region in which the envelope of the oscillating signals is linear, see e.g. figure 4.

Based on the results above, we conclude that the fine grid resolutions in table 2 are sufficient to study the inherently unsteady dynamics of the three-dimensional flow fields in the present cases.

4. Effects of ellipticity

Honji (1981) named the pattern that arose from the three-dimensional instability streaked flow due to the characteristic bands that his flow visualizations revealed. Later, subsequent investigations reported mushroom-like structures in the visualizations over planes normal to the cylinder wall (see e.g. Sarpkaya 1986; Tatsuno & Bearman 1990; Zhang & Dalton 1999; An *et al.* 2011; Suthon & Dalton 2012). If, as theoretically predicted by Hall (1984), the same type of centrifugal instability occurs in the oscillating flow past elliptic cylinders, similar vortical structures consisting of pairs of counter-rotating vortices are expected.

Figure 5 shows snapshots at phase $T/4$ of the instantaneous isosurfaces of streamwise vorticity ω_x for the different values of Λ considered in this study. For $\Lambda = 2/3$ and above we observe the same distinctive mushroom-like structures reported by previous authors (Zhang & Dalton 1999; Sarpkaya 2002; An *et al.* 2011; Suthon & Dalton 2011). Staggered rows of counter-rotating vortices are seen on each side of the cylinder. When $\Lambda = 1$ the vortices are equally sized and evenly distributed, in good

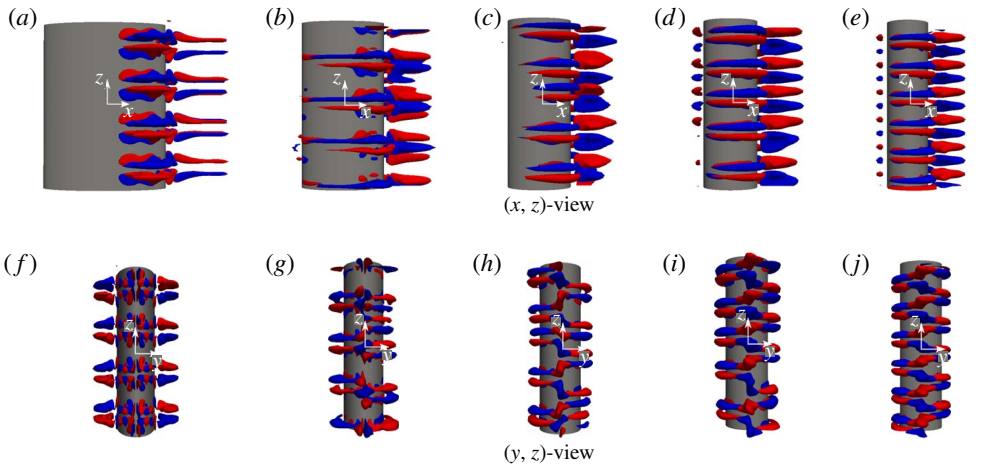

FIGURE 5. Instantaneous isosurfaces of streamwise vorticity $\omega_x = \pm 0.5$ at phase $T/4$ for aspect ratios of $\Lambda = 1/3$ (a,f), $1/2$ (b,g), $2/3$ (c,h), $\sqrt{3/5}$ (d,i) and 1 (e,j). Red isosurfaces correspond to positive vorticity and blue to negative vorticity. Corresponding cases in table 1 are C_{1c}, C_2, C_3, C_4 and C_5.

agreement with the observations by An *et al.* (2011); six pairs of counter-rotating vortices at each side give a wavelength of $0.67b$, whereas for $\Lambda = 2/3$ and $\sqrt{3/5}$ the wavelength increases to $0.8b$. The (y, z)-views for $\Lambda = 2/3$ and above show that tubes on one side of the cylinder join the tubes with same vorticity sign at the opposite side of the cylinder, with opposite vorticity isosurfaces connecting them at the stagnation line as observed by Suthon & Dalton (2012) for $\Lambda = 1$. As Λ decreases the size of the flow structures as well as their distribution along the span varies to some extent, indicating that the structures are not fully stable. Although according to Hall's theory the instability location for $\Lambda = 2/3$ is about $\phi = \pi/4$ (figure 1b), the upper and lower branches of the instability curves in figure 1(a) are very close to each other, and the expected effects of ellipticity are therefore modest.

When $\Lambda = 1/2$ the distribution of the flow structures is uneven, and the wavelength is somewhere between $0.8b$ and $1.0b$. Shifting of flow structures towards the stagnation line on the right in the (x, z)-views indicates that the effects of ellipticity start to be more pronounced, and agrees well with Hall's theory. The (y, z)-view for the lowest aspect ratio considered, $\Lambda = 1/3$, shows that the bands of vorticity isosurfaces with opposite sign at each side of the cylinder are aligned, contrary to the staggered rows seen for instance at $\Lambda = 1$. Next to the stagnation line the pattern of the vortical structures for $\Lambda = 1/3$ is distinctly different from that seen at higher Λ. The streamwise vortices for $\Lambda = 1/3$ exhibit a flattened rather than the characteristic tubular shape of the Honji vortices. Suthon & Dalton (2011) described the formation of the vortex pairs for a circular cylinder as spanwise vorticity ω_z which undergoes stretching and reorientation into streamwise and cross-stream vorticity. It is plausible that this same process is responsible for the generation of the vortical structures at $\Lambda = 1/3$, however, as Λ decreases the eccentricity of the ellipse increases, giving rise to these characteristic spanwise vortical structures.

The isosurfaces of spanwise vorticity ω_z in figure 6 exhibit the same rib-like layers mentioned above for cases $\Lambda = 2/3$, $\sqrt{3/5}$ and 1, and agree well with the visualizations reported by An *et al.* (2011) for circular cylinders. In addition to the

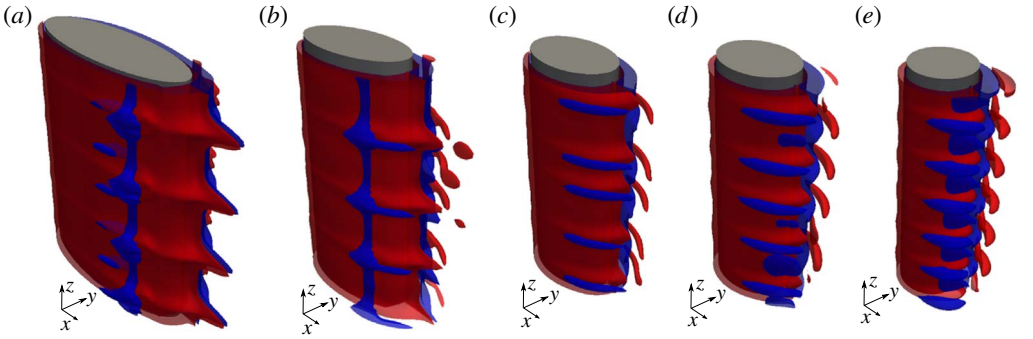

FIGURE 6. Perspective view of the spanwise vorticity $\omega_z = \pm 1.0$ at phase $T/4$ for aspect ratios of $\Lambda = 1/3$ (*a*), 1/2 (*b*), 2/3 (*c*), $\sqrt{3/5}$ (*d*) and 1 (*e*). Red isosurfaces correspond to positive vorticity and blue to negative vorticity. Corresponding cases in table 1 are C_{1c}, C_2, C_3, C_4 and C_5.

characteristic undulations in the layers of vorticity, we observe two deformed tubes with their cores aligned with the axis of the cylinder for the cases with $\Lambda = 1/3$ and 1/2. The emergence of these structures at low Λ is an obvious consequence of the increased eccentricity of the ellipses.

Contrary to the present study, Yang (2014) focussed on modest eccentricities $\Lambda \gtrsim 0.866$, i.e. well above the critical aspect ratio $\sqrt{3/5} \approx 0.775$ at which the instability diagram in figure 1(*a*) bifurcates. The only exceptions were the cross-sections $\Lambda = 0.766$ and 0.5 that were studied at the relatively high $\beta = 400$. Although Yang's $KC = 2.0$ matches that used for cases C_2 and C_4, the twice as high Stokes number β makes the resulting flow fields qualitatively different.

5. Development of the flow structures for $\Lambda = 1/3$

In the following we examine results for $\Lambda = 1/3$, $KC = 2$, and varying $\beta = 200$, 300, 400, 500 and 600. This cylinder configuration has a relatively low aspect ratio Λ which gives rise to peculiar vortex patterns compared to other configurations with more modest eccentricity.

The lack of previous physical observations of the instabilities generated by oscillating flow past an elliptic cylinder led us to conduct extensive spatio-temporal sampling. First, the time evolution of the instability was tracked with a sampling set consisting of 10 confocal ellipses, each with 60 sampling points equidistant at an angle of 6°, yielding a total of 600 sampling points in each (x, y)-plane. In the axial direction samples were taken at 41 equidistant (x, y)-planes separated by $0.1b$, thus the total number of sampling points is 24 600. The time windows for the sampling varied depending on how fast the instabilities develop. For case C_{1a}, a total of 30 cycles were sampled; for case C_{1b} 80 cycles; and for cases C_{1c} to C_{1e} 60 cycles.

The time series portraying the evolution of the three-dimensionality of the flow for cases C_{1b}–C_{1e} are shown in figure 7. A line parallel to the cylinder axis at the instability location ϕ_2 given by (1.3) and at a distance from the cylinder of $0.2b$ in the wall-normal direction was chosen to show the temporal and spatial development of the spanwise velocity w. The emergence of this velocity component renders the flow three-dimensional, indicating the occurrence of the primary instability predicted by Hall (1984). At $\beta = 200$ no traces of spanwise velocity w were observed, thus the

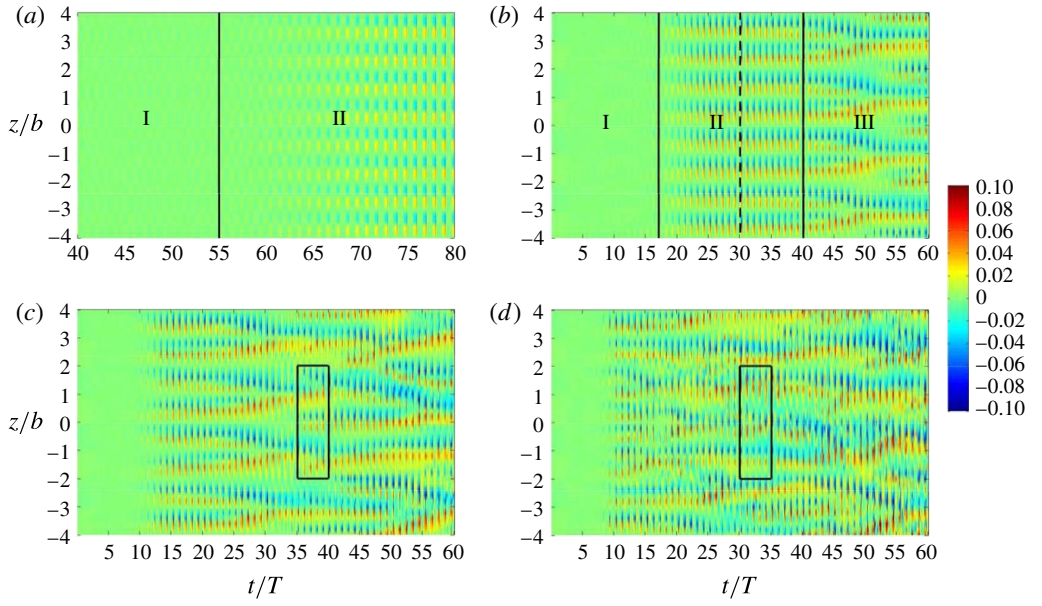

FIGURE 7. Time evolution of the spanwise velocity component w for $\Lambda = 1/3$ and $KC = 2$. Roman numerals I, II and III denote the different phases identified by Yang *et al.* (2014) for the Honji instability on a circular cylinder. The boxes in (*c*,*d*) demarcate the regions for sampling during five periods (figures 20 and 21). (*a*) $\beta = 300$; (*b*) $\beta = 400$, with the dashed line indicating time for the sampling during one period in figure 18; (*c*) $\beta = 500$; and (*d*) $\beta = 600$.

flow is two-dimensional. For $\beta = 300$ and above, characteristic strips similar to those reported by An *et al.* (2011) for a circular cylinder are observed. This streaked flow pattern resembles that first observed by Honji (1981) in the flow around an oscillating circular cylinder, which gives rise to pairs of counter-rotating vortices or mushroom-shaped coherent structures (see e.g. Sarpkaya 2002; Suthon & Dalton 2011). However, since the bluff body involved in the present study is an elliptic cylinder, we avoid denoting this a Honji instability.

Case C_{1b} (figure 7*a*) starts to exhibit three-dimensionality after approximately 55 oscillation cycles, and the spanwise velocity w grows at a relatively slow rate of 0.0031. Two phases I and II can be distinguished in this case, according to the classification previously presented by Yang *et al.* (2014). Phase I is characterized by the absence of three-dimensional instabilities, as is the case for C_{1a}, whereas in phase II the instabilities grow and develop into a stable structure; essentially after approximately 75 cycles for $\beta = 300$. When β increases to 400 (figure 7*b*) the instability grows at a faster rate 0.0123. Phase I lasts about 17 cycles for this case, and the strips develop into a stable structure thereafter (phase II). However, a third phase III characterized by rearrangements of the strips is observed in this case after approximately 40 cycles. A fundamental difference with the instability of the flow past a circular cylinder (and elliptic cylinders with low ellipticity) is that the Honji vortices are sustained throughout one period of oscillation (Sarpkaya 2002; An *et al.* 2011; Suthon & Dalton 2011), whereas the three-dimensional instability in the present case with $\Lambda = 1/3$ grows and decays periodically.

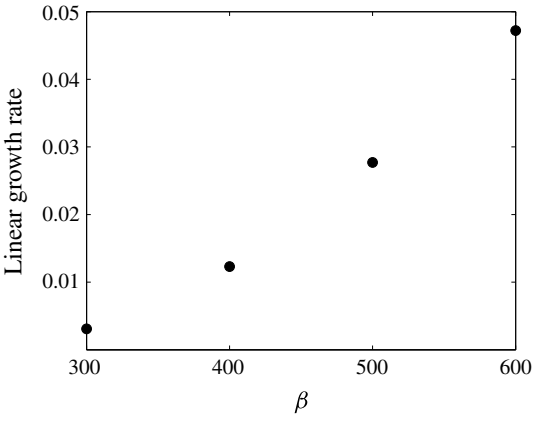

FIGURE 8. Estimated growth rates for the Stokes numbers considered in the simulations with $KC = 2$ and $\Lambda = 1/3$.

Increasing β further for a given KC leads to complex interactions between the flow structures. Case C_{1d} in figure 7(*c*) exhibits an early development of the three-dimensional flow ($\approx$10 cycles) with a linear growth rate of 0.0277, and then stable structures, depicted by the parallel strips, for approximately five cycles. This is followed by a further development into more complex flow involving rearrangements along the span of the cylinder. A similar development of the flow structures has been reported by An *et al.* (2011) for circular cylinders, which involves merging and annihilation of the vortices. For a circular cylinder, experimental observations by Honji (1981) and Sarpkaya (2006) report transition to turbulence when $KC = 2$ and $\beta = 580$. This was confirmed by the direct numerical simulations of An *et al.* (2011) for $KC = 2$ and $\beta = 600$, where an irregular flow pattern and abrupt changes in the flow structures over time intervals as short as one cycle were reported. In figure 7(*d*), the same (KC, β)-combination of parameters for an elliptic cylinder with aspect ratio $\Lambda = 1/3$ gives rise to an irregular flow pattern and more frequent reorganizations of the strips than at $\beta = 500$. The linear growth rate during the initial development of the three-dimensional flow is 0.0472. Despite this apparently chaotic behaviour, the flow still retains the basic paired structure observed at lower β and it cannot be classified as turbulent.

The estimated growth rates for the different Stokes numbers are shown in figure 8. For this particular aspect ratio ($\Lambda = 1/3$) and $KC = 2$, the growth rate increases monotonically with β, i.e. as the stabilizing influence of the fluid viscosity is reduced. Moreover, by extrapolating the growth rate to zero using a second-order polynomial, the critical β-value $\approx$247.4 for the onset of the instability is obtained.

Further information about the time evolution of the instability can be obtained by plotting the velocity traces at a particular spanwise location. This allows us to compare the strength of the three-dimensional flow for different values of β, and to examine the periodicity of the flow at different locations. In figure 9 two characteristic spanwise locations were selected for each case in order to visualize the traces of w during five cycles; the two lines aim to cut the positive and negative part of the strips, and for $\beta = 400$ the time window is located within phase II. In addition to the data at the primary instability location ϕ_2, traces at $\phi_1 = \pi/2$ corresponding to the upper branch of the cusp-shaped curve shown in figure 1(*a*) are also included. We recall that for

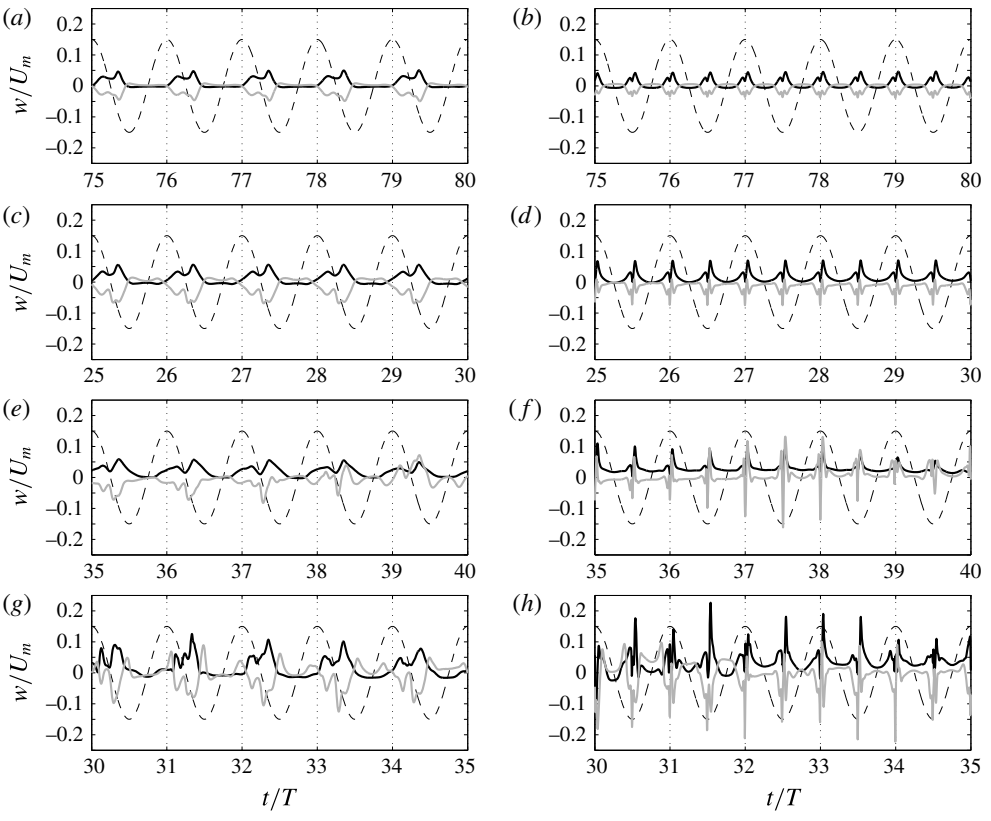

FIGURE 9. Time history of the spanwise velocity component w over five cycles for $\Lambda = 1/3$, $KC = 2$ and $\beta = 300$ (a,b), 400 (c,d), 500 (e,f) and 600 (g,h). Two samples inside the strip pairs shown in figure 7 are selected, and samples are taken at $0.2b$ from the cylinder and at critical angles $\phi_2 = 16.8°$ (a,c,e,g) and $\phi_1 = 90°$ (b,d,f,h). Samples were aimed to trace the two poles of a vortex pair, measuring positive (black lines) and negative (grey lines) velocities. The dashed curves indicate the time variation of the imposed oscillating flow U.

a circular cylinder ($\Lambda = 1$) and elliptic cylinders with $\Lambda > \sqrt{3/5}$ this is the location where the Honji instability is initialized. In addition, the dashed curves in figure 9 depict the time variation of the imposed oscillations.

The spanwise velocity traces when $\beta = 300$ and 400 at ϕ_2 exhibit a main peak of about 5 % the free-stream velocity preceded by a secondary peak of lower magnitude. These peaks are synchronized with the ambient flow with a phase shift of approximately $\pi/4$. A similar behaviour is observed at $\beta = 500$ and 600, but the traces are more irregular with amplitudes of approximately 10 % the incoming flow in this case. Overall, the three-dimensional instability at this location reaches its maximum intensity during flow reversal at times $t = T/4$ and then decays to zero at $\approx T/2$. At ϕ_1 we observe two peaks within a cycle which are phase aligned with the ambient flow. The intensity of the three-dimensional flow grows from $\approx$5 % of the velocity U_m at $\beta = 300$ to approximately 20 % of U_m at $\beta = 600$. Indeed, for $\beta = 600$ the intensity of w at ϕ_1 exceeds that at ϕ_2, suggesting a transition in the primary instability location from (ϕ_2, ϕ_3) to ϕ_1 (see figure 1).

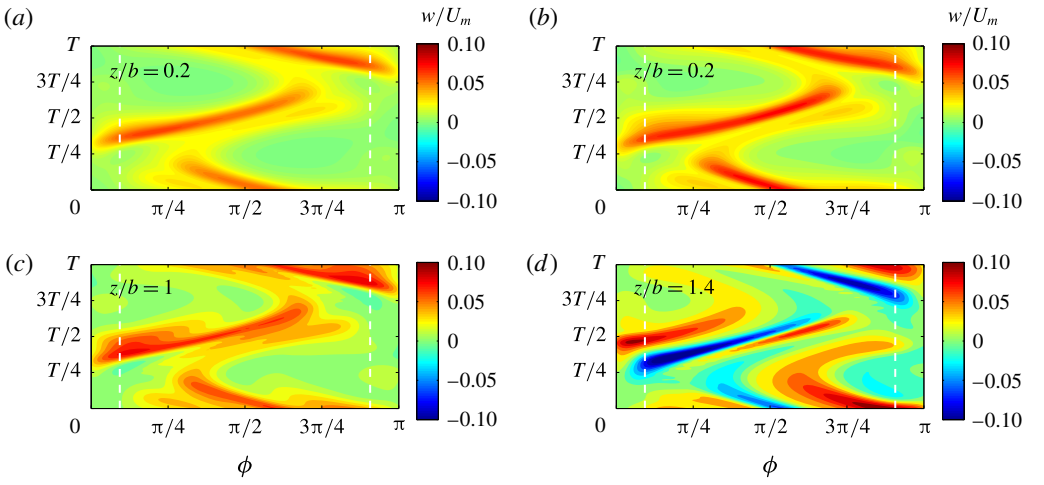

FIGURE 10. Temporal evolution of the spanwise velocity w during one cycle along the upper half of the elliptical cross-section for $\Lambda = 1/3$, $KC = 2$ and $\beta = 300$ (*a*), 400 (*b*), 500 (*c*) and 600 (*d*). The samples are taken at a wall-normal distance of $0.1b$, and white dashed lines denote the critical angles $\phi_2 = 16.8°$ and $\phi_3 = 163.2°$.

An interesting result from Hall's instability analysis is the cusp-shaped curve for some orientations of an elliptic cylinder (see figure 1*a*), and the gradual displacement of the instability points from the shoulders of the cylinder towards the stagnation points as Λ decreases (see figure 1*b*). In order to validate Hall's theory, we sampled the spanwise velocity w around the elliptic cross-section at a normal distance of $0.1b$, where the boundary-layer velocities are around their maxima. The dashed lines in figure 10 denote the critical angles $\phi_2 = 16.8°$ and $\phi_3 = 163.2°$ given by Hall's theory for the primary instability, i.e. (1.3). The spatio-temporal evolution of the spanwise velocity w has been tracked in this way throughout one period T for $\beta = 300$–600 at the spanwise locations z indicated in the plots.

Figure 10 shows similar w-evolution for $\beta = 300$, 400 and 500. The instability is triggered around ϕ_2 at phase $T/4$, and then the initial eruption of axial velocity is pushed around the elliptic cylinder for approximately half a cycle, passing through the secondary instability location ϕ_1 during this process. Emergence of the axial velocity around ϕ_3 occurs around phase $3T/4$ and then moves in the opposite direction (left) towards ϕ_2. This swinging displacement of the instability along the walls of the elliptical cross-section explains the two peaks in one cycle at ϕ_1 seen in figure 9.

For $\beta = 600$ (figure 10*d*) the evolution of w-bursts along the wall of the elliptic cylinder exhibits similar properties as those observed at lower β. However the magnitude of the spanwise velocity in this case is more pronounced. Moreover, the symmetry exhibited at lower β is absent in this high Stokes number case due to the dramatic changes in the flow structures depicted by figure 7(*d*).

The overall agreement with Hall's theory is very good indeed when it comes to the prediction of the eruptions of three-dimensional flow at ϕ_2 and ϕ_3. Additionally the results presented in figure 10 show the life of this primary instability throughout one time cycle T and its initiation at phase $T/4$, which corresponds to flow reversal.

Next we explore the properties of the flow in cross-sectional (x, y)-planes during a half-cycle for $\beta = 200$–600; all the snapshots are taken at the same spanwise position

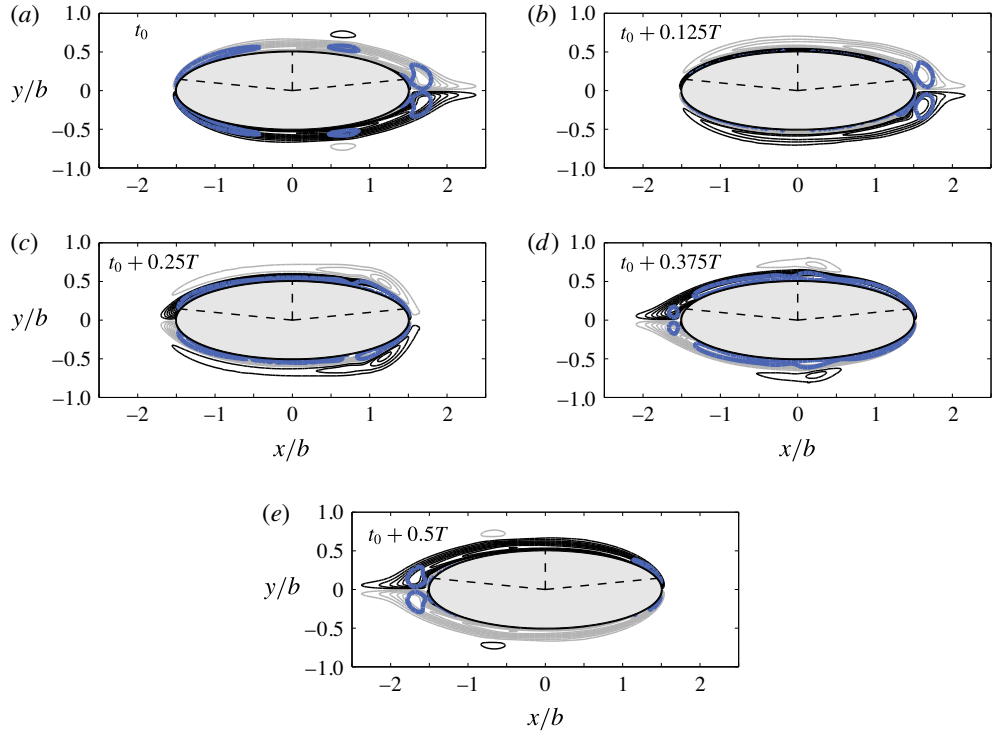

FIGURE 11. (Colour online) Contours of normalized spanwise vorticity ω_z (black, positive, and grey, negative values) and the second largest eigenvalue λ_2 (thick contours to denote vortex cores) during half a period $T/2$ at intervals of $T/8$. In all the plots $|\omega_z b/U_m| = 10$ with $\Delta\omega_z b/U_m = 1$, and $\lambda_2 = -2$. Snapshots taken at $z/b = 0.4$. Case C_{1a} with $\Lambda = 1/3$, $KC = 2$ and $\beta = 200$.

$z/b = 0.4$. At low β the flow is symmetrical with respect to the (x, z)-plane and essentially two-dimensional along the cylinder axis. This is evident in figure 11, in which contour lines of ω_z at $\beta = 200$ are plotted together with contours of the parameter λ_2 to identify vortex cores (Jeong & Hussain 1995); black lines indicate positive vorticity and grey lines negative vorticity. The parameter λ_2 represents the location of vortex cores, and is defined as the second largest eigenvalue of the tensor $\boldsymbol{S}^2 + \boldsymbol{\Omega}^2$, where $\boldsymbol{S}$ and $\boldsymbol{\Omega}$ are the symmetric and antisymmetric parts of the velocity-gradient tensor, respectively. Contours of vorticity allow identification of the Stokes layer of opposite vorticity, clearly seen at $t_0 + 0.125T$ and $t_0 + 0.25T$ in figure 11. Two pairs of vortices with opposite signs develop symmetrically during a half-cycle close to the stagnation points. A similar development of symmetrical pairs of vortices has been reported for a circular cylinder (see e.g. Tatsuno & Bearman 1990; Zhang & Dalton 1999). These regions of concentrated vorticity within the pair of vortices are convected along the cylinder by the ambient flow, however they die out before reaching the opposite end of the ellipse as they mix with vorticity of opposite sign in the cylinder boundary layer (figure 11 at phases t_0 and $t_0 + 0.5T$). Apart from these vortex pairs there is no evidence of massive separation involving vortex shedding and large excursions from the wall.

An interesting aspect of the flow around elliptic cylinders is the change in the shape of the bluff body as the parameter Λ decreases (see figure 2), since this includes the problems of the circular cylinder ($\Lambda = 1$) and a flat plate ($\Lambda = 0$) as limiting cases.

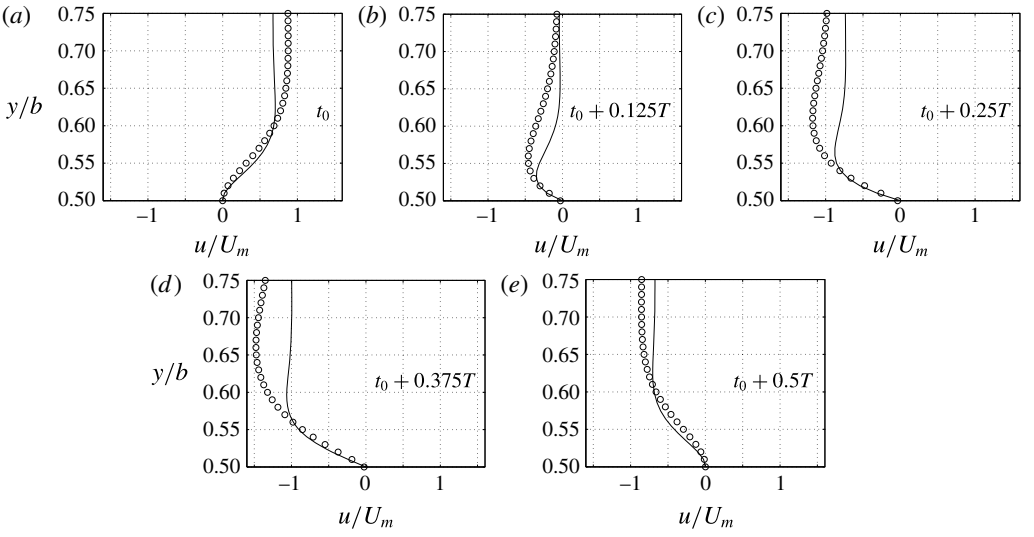

FIGURE 12. Velocity profiles during half a period taken at $\phi_2 = \pi/2$. Case with $\Lambda = 1/3$, $KC = 2$ and $\beta = 200$ ($\circ\circ\circ$) and Stokes' theoretical solution (5.1) for oscillating flow over a fixed wall ($-$).

Stokes provided the first theoretical solution of the sinusoidal oscillatory motion of unbounded fluid over an infinite flat plate, which is known as Stokes' second problem. Although still far from being a flat plate, an elliptic cross-section with aspect ratio $\Lambda = 1/3$ differs considerably from a circular cross-section, therefore a comparison with Stokes' theoretical solution is meaningful in the present context.

The solution for oscillating flow over a fixed and infinitely long wall (White 2006) with free-stream velocity $U_m \cos(2\pi t/T)$ is given by

$$\frac{u(y,\,t)}{U_m} = \cos\left(2\pi\frac{t}{T}\right) - \exp(-\eta)\cos\left(2\pi\frac{t}{T} - \eta\right), \tag{5.1}$$

with $\eta = \sqrt{\pi\beta}\,y/b$. The thickness δ of the oscillating boundary layer when $\exp(-\eta) = 0.01$, i.e. $\eta \approx 4.6$, is

$$\frac{\delta}{b} \approx \frac{4.6}{\sqrt{\pi\beta}}. \tag{5.2}$$

Figure 12 shows the velocity profiles for $\beta = 200$ taken at the upper shoulder of the ellipse ($\phi = \pi/2$) together with Stokes' theoretical solution; the profiles are plotted at the same phases as those in figure 11. Clearly, at a distance of $0.05b$ from the wall the agreement between the simulation and the theory is very good. However, the overshooting higher up in the boundary layer is always larger in the simulations. The theoretical prediction of the boundary-layer thickness for a flat plate at $\beta = 200$ yields $\delta/b = 0.184$, differing substantially from the simulations because, in this case, the velocity takes longer to decay due to the perturbation induced by the elliptical cross-section. It is expected that the agreement with the theoretical predictions will improve as the shape parameter Λ decreases. Nevertheless the vorticity attains very low values at $0.2b$ from the wall due to the low gradients in the velocity profiles in figure 12.

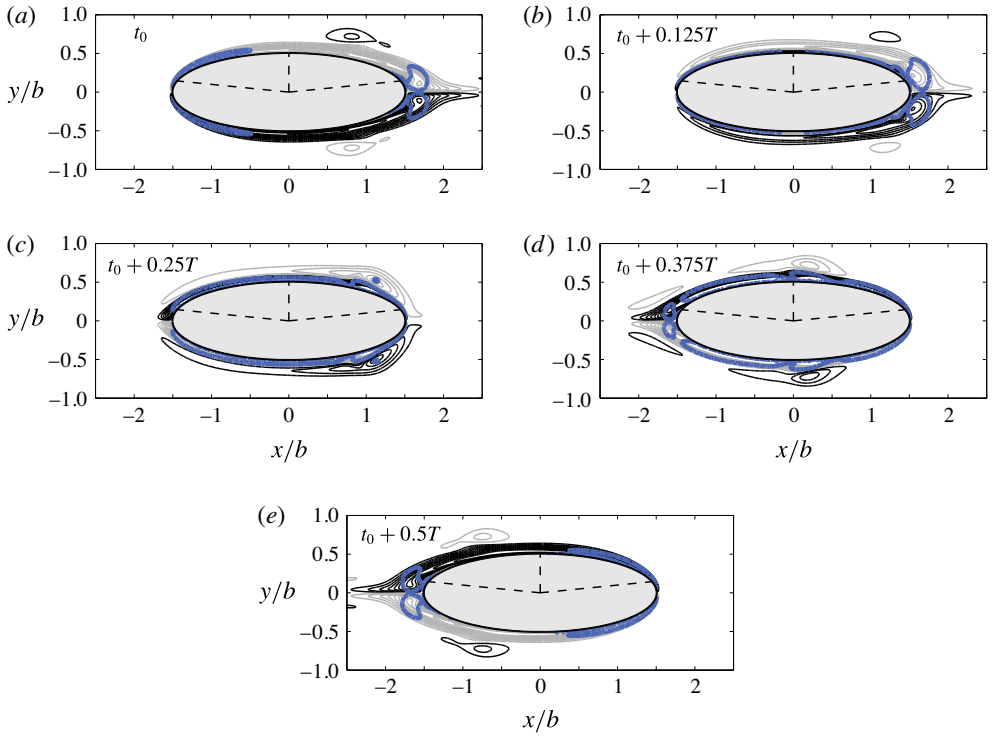

FIGURE 13. (Colour online) As figure 11 but $\beta = 300$.

The velocity profiles at phases t_0 and $t_0 + 0.5T$ give the impression that separation occurs at the wall. However, the region where ω_z vanishes (or equivalently the wall shear stresses vanish) does not necessarily correspond to separation point as in steady approaching flow. The largest difference in velocity between the simulations and the flat-plate solution occurs at phase $t_0 + 0.375T$, when the magnitude of free-stream velocity reaches its maximum value U_m. Here the magnitude of the velocities of the flow around the elliptic cylinder exceeds those of the flat plate by about $0.5U_m$. When it comes to the distribution of the velocities the results in figure 12 exhibit good qualitative agreement.

From the comparisons in figure 12 we learned that the simple analytic solution (5.1) for oscillating flow over an infinitely long flat plate compares surprisingly well with the computed velocity profiles at $\phi = 90°$ on the curved surface of the elliptic cylinder. This demonstrates not only that the effect of the local curvature of the ellipse is almost negligible, but also that the vortices in the stagnation regions seen in figure 11 have a negligible effect on the flow field at the shoulders for this particular aspect ratio. For even lower aspect ratios, i.e. $\Lambda < 1/3$, an even closer correspondence between the flow field around the ellipse and the analytical flat-plate solution is expected.

At higher β the flow in the cross-sectional plane retains the characteristics observed at $\beta = 200$ when it concerns the generation of a counter-rotating vortex pair at each half-cycle (see for instance figures 13 and 14). The amount of vorticity within the two distinct lobes convected along the cylinder walls increases with β. Indeed, at $\beta = 400$ there is still some vorticity remaining at phase $t_0 + 0.25T$ after flow reversal has started and the counter-rotating vortex pair at the right end is convected

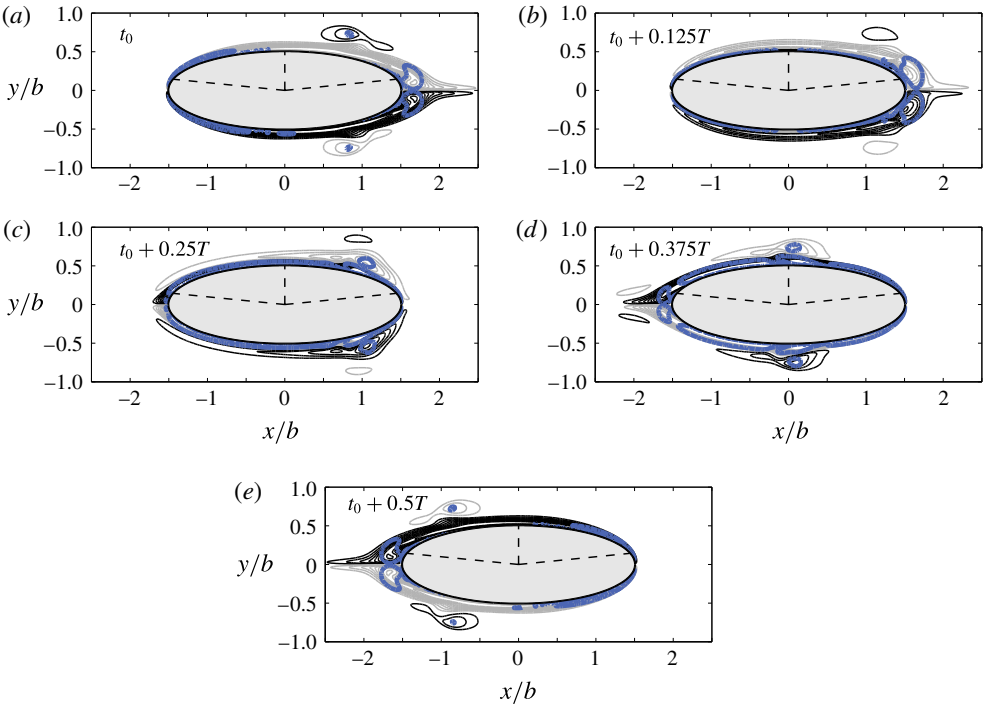

FIGURE 14. (Colour online) As figure 11 but $\beta = 400$.

in the negative x-direction. These structures also keep the same relative locations while moving left and right as the flow direction changes. At phase $t_0 + 0.125T$ the free-stream velocity is close to zero and the acceleration of the flow is a maximum, resulting in expanded vortex cores. Although the structure of the flow at $\beta = 300$ and 400 resembles remarkably that at $\beta = 200$ in figure 11, the structure of the flow is now three-dimensional due to the instability in the boundary-layer flow (figure 7*a*,*b*). This similarity in the distribution of the ω_z-contours indicates that two-dimensional flow dominates; moreover the flow retains the symmetry about the (x, z)-plane. The phase at which the structures are largest ($t_0 + 0.125T$) coincides with the occurrence of the three-dimensional instability (figure 9). It is also clear from figures 13 and 14 that no vortex shedding occurs.

Next we proceed to explore the properties of the cross-sectional flow at $\beta = 500$ and 600 in figures 15 and 16, respectively. At higher β the Stokes layers become thinner in accordance with the estimate (5.2) while preserving the main flow structure with counter-rotating vortex pairs generated each half-cycle. The symmetry about the (x, z)-plane is now broken, which is expected from the spanwise variations of the flow previously seen in figure 7(*c*,*d*). At $\beta = 500$ in figure 15, the two distinct lobes convected along the cylinder walls shrink in size and concentrate more vorticity than at lower β. Despite this increase in vortex strength the lobes are annihilated at phase $t_0 + 0.25T$ due to strong opposite vorticity travelling in the opposite direction. The situation is different for $\beta = 600$ in figure 16, where detached vortex cores give evidence of separated flow from the cylinder walls; this is clear from the plots at phases t_0 and $t_0 + 0.125T$. An interesting interaction between the weakened vortex travelling to the right and the stronger vortex travelling to the left is seen starting

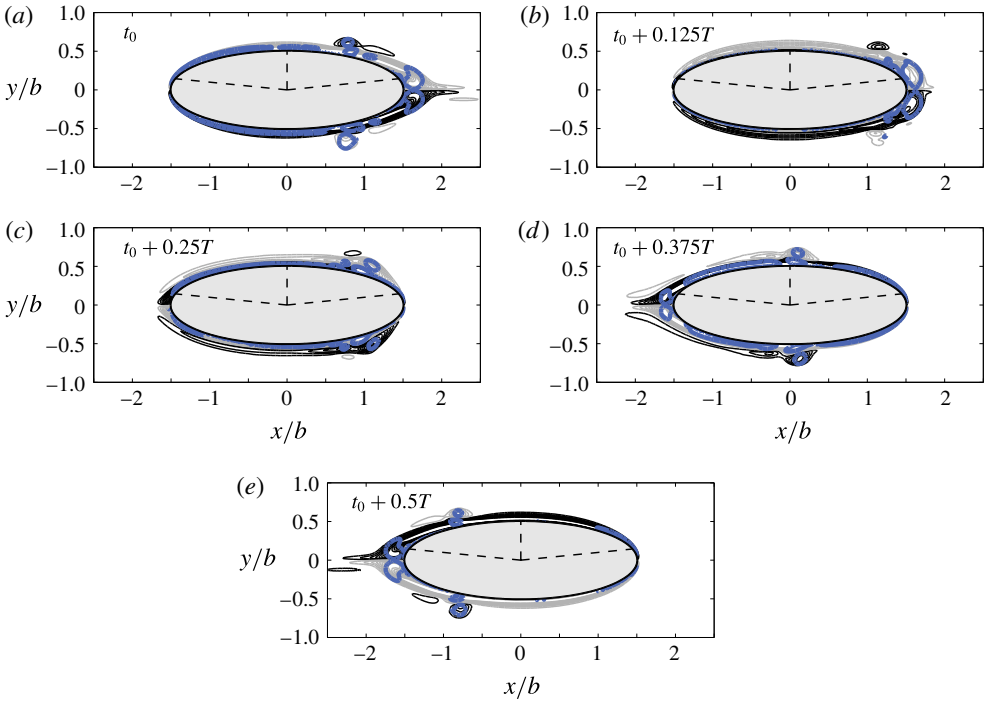

FIGURE 15. (Colour online) As figure 11 but $\beta = 500$.

from phase $t_0 + 0.125T$ in the upper half of the ellipse. At phase $t_0 + 0.25T$ the two vortices collide at about $x/b = 1$, and later at phase $t_0 + 0.375T$ we observe at $\phi = \pi/2$ that the two vorticity regions have merged, resulting in filamentation of the region with positive vorticity. Detached vorticity regions at both tips of the elliptic cylinder can also be observed in figure 16.

In order to explore the development of the three-dimensional instability, we use vorticity contours at vertical planes in the vicinity of the location where the three-dimensional instability arises. We start by looking at stable structures in the phase II for $\beta = 300$ and 400 indicated in figure 7(*a*,*b*), respectively. Previous observations of equivalent structures on circular cylinders have shown distinctive mushroom-like shapes corresponding to vortex pairs (see e.g. Sarpkaya 2002; An *et al.* 2011; Suthon & Dalton 2011) which are referred to as Honji vortices.

Figures 17 and 18 show the projected normalized vorticity $\omega_{\hat{n}}$ over a cross-section located at the critical angle ϕ_2 for $\beta = 300$ and 400, respectively. The evolution of the three-dimensional structures is followed through one cycle because, contrary to the Honji vortices, the structures at the elliptic cylinder with $\Lambda = 1/3$ are not sustained throughout one cycle. In accordance with Hall's theory, during the first half-cycle the three-dimensional structures grow and develop at the location ϕ_2, and the same process repeats itself during the second half-cycle at ϕ_3. At phase t_0 we observe a pair of counter-rotating vortices and regions of relatively weak vorticity next to the wall. Phase $t_0 + 0.125T$ corresponds to the region of maximum flow acceleration and enlargement of the vortex cores in the cross-sectional planes, and here the flow structures in figures 17 and 18 clearly concentrate more vorticity. The position of the vortex pair is shifted away from the wall, and a unique pattern consisting of eight

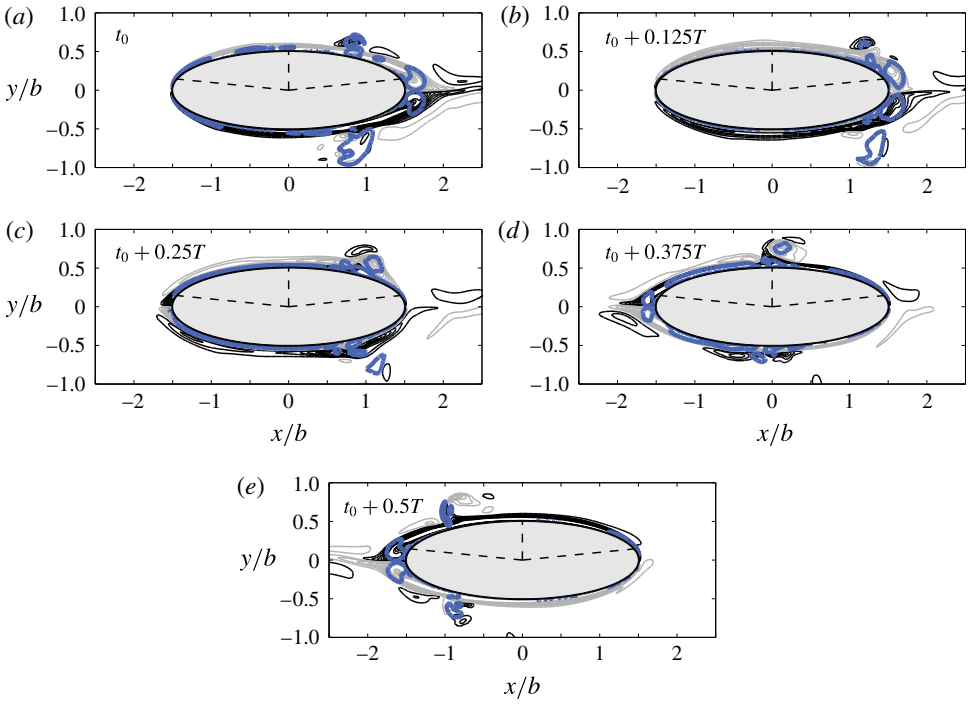

FIGURE 16. (Colour online) As figure 11 but $\beta = 600$.

cells with opposite vorticity sign is observed below the vortex pair. Then at phase $t_0 + 0.25T$ the main vortex pair approaches the wall and intense vorticity regions are seen next to the wall; at this stage we have flow reversal, and the development of the structures on the opposite side of the ellipse, at ϕ_3, begins. Thereafter the free-stream velocity reaches its maximum magnitude at phase $t_0 + 0.375T$, and the vortex pair gradually decays in the following phases until the growth of the vortex pairs starts again and the whole process repeats itself. Dramatic growth of the instability will start again from phase $t_0 + 0.875T$, which is the stage at which the free-stream velocity reaches its maximum magnitude. In the same way as for a circular cylinder, it is clearly the vorticity in the boundary layer that provides the mechanical energy required to sustain the upper counter-rotating vortex pair.

Figures 17 and 18 show the same structure of the evolution of the three-dimensional instability at $\beta = 300$ and 400, the only difference being the increase in the magnitude of the vorticity at $\beta = 400$. In order to quantify this the vorticity has been integrated over the right half of the planes in figures 17 and 18 to obtain the circulation Γ; this is also an alternative way to portray the evolution in time of the three-dimensional instability. Figure 19 shows that the magnitude of the circulation for $\beta = 400$ is about 30 % larger than that at $\beta = 300$ from phase t_0 to $t_0 + T/4$. Then the circulation decays rapidly, reaching almost zero values at $t_0 + T/2$ and $t_0 + 5T/8$ for both $\beta = 300$ and 400. Then the three-dimensional instability starts growing again, with increasing differences in circulation between $\beta = 300$ and 400 as the flow reverses to the positive x-direction.

The properties of the flow structures when β increases to 500 and 600 are explored in figures 20 and 21, respectively. In these flow regimes the structures are expected

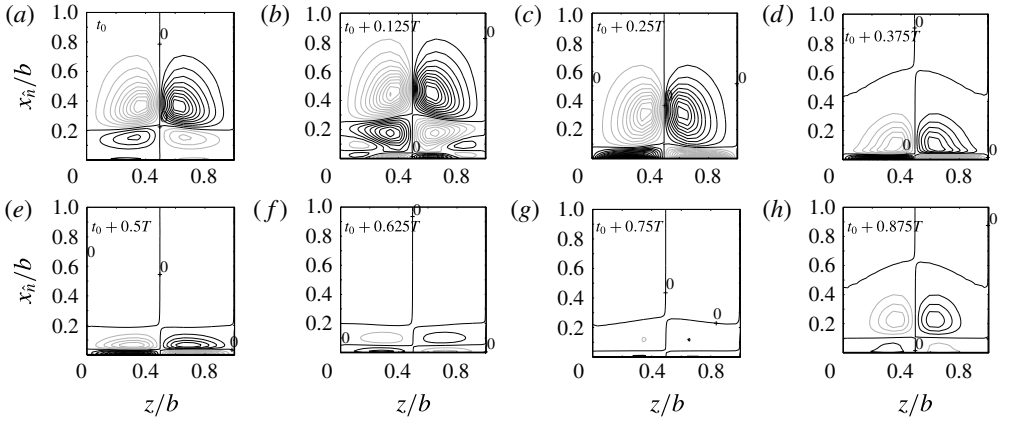

FIGURE 17. Projected normalized vorticity $\omega_{\hat{n}}$ over a cross-section located at the critical angle ϕ_2; eight different phases at intervals of $\Delta T = 0.125T$ during a period T. In all the plots $|\omega_{\hat{n}} b/U_m| = 2$ with $\Delta\omega_{\hat{n}} b/U_m = 0.1$. Black contours denote positive vorticity and grey contours negative vorticity. Case with $\Lambda = 1/3$, $KC = 2$ and $\beta = 300$.

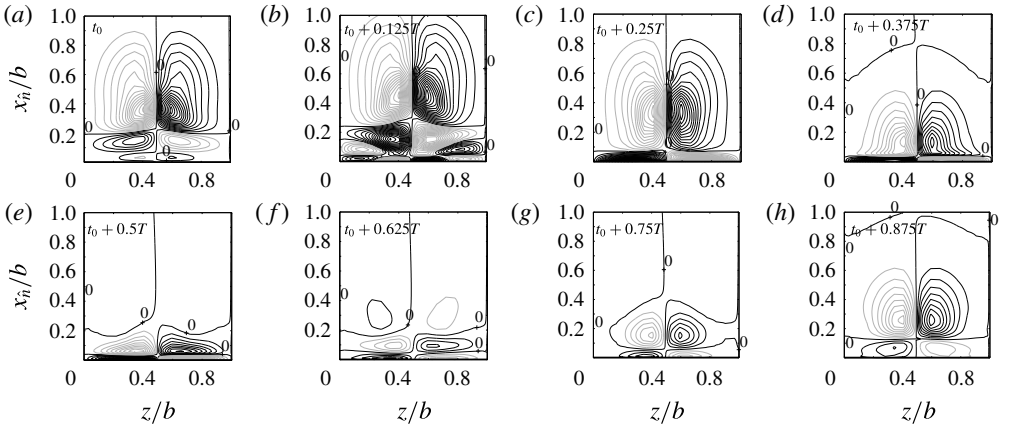

FIGURE 18. As figure 17 but $\beta = 400$.

to be unstable according to the information conveyed by figure 7(*c*,*d*). Several events where the strips merge can be observed, indicating coalescence of two flow structures. Using high-speed imagers and laser-induced fluorescence, Sarpkaya (2002) observed such merging events in the sinusoidal oscillatory flow over a circular cylinder. Subsequently An *et al.* (2011) examined the evolution of the interaction between the mushroom-shaped structures by means of direct numerical simulations.

In figures 20 and 21 the vorticity $\omega_{\hat{n}}$ normal to a plane oriented at $\phi = 22.5°$ has been plotted over five periods all at the same phase $T/4$. The sampling windows are indicated by the boxes in figure 7(*c*,*d*) for $\beta = 500$ and 600, respectively. At $t = 35.25T$ in figure 20 we observe five pairs of counter-rotating vortices along a spanwise length of $4b$. The structure located at midspan ($z/b = 0$) remains locked at this position as time advances, exhibiting only minor alterations in its shape. In the left part of the plots we observe two structures $P1$ and $P2$ at $t = 35.25T$ approaching each other. Positive vorticity in $P1$ and negative vorticity in $P2$ cancel each other out during this

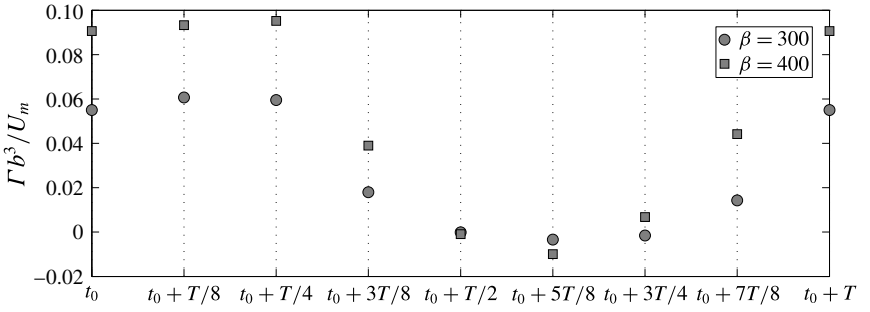

FIGURE 19. Integrated normalized circulation Γ over a cross-section located at the critical angle ϕ_2. The integration is done from $z/b = 0.5$ to 1.0 in figures 17 and 18. Cases with $\Lambda = 1/3$, $KC = 2$, and $\beta = 300$ and $\beta = 400$.

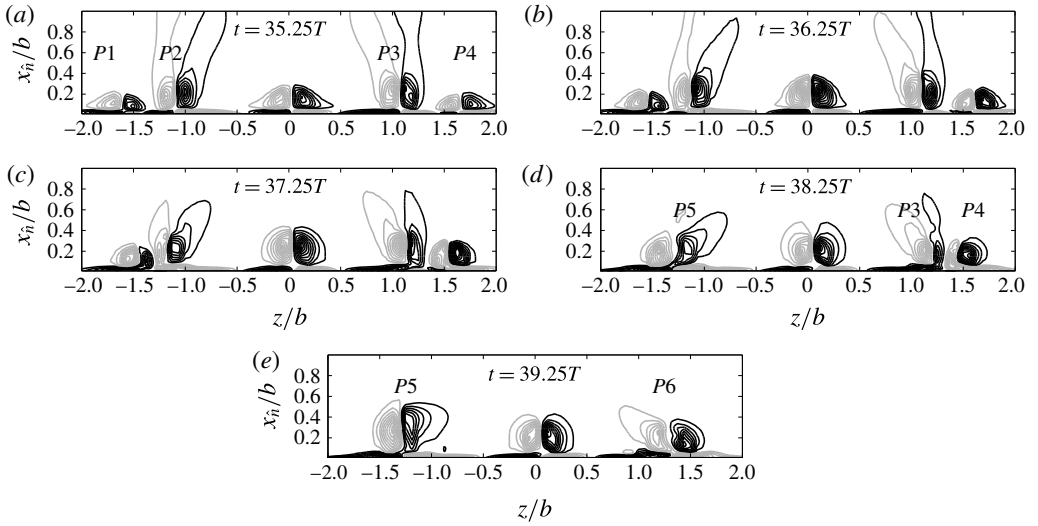

FIGURE 20. Time evolution of the projected normalized vorticity $\omega_{\hat{n}}$ over a cross-section located at $\phi = 22.5°$ ($\approx 6°$ anticlockwise from the critical angle ϕ_2). Consecutive snapshots taken at phase $T/4$. In all the plots $|\omega_{\hat{n}} b/U_m| = 2$ with $\Delta\omega_{\hat{n}} b/U_m = 0.1$. Case with $\Lambda = 1/3$, $KC = 2$ and $\beta = 500$.

merging process, and this blending results in a new vortex pair $P5$ at $t = 38.25T$. A similar situation is observed to the right part of the panels, where the pairs $P3$ and $P4$ have merged at $t = 39.25T$, giving rise to the new vortex pair $P6$.

Vortex pairs are still seen at $\beta = 600$, however the irregularity of their shape increases considerably (figure 21). Furthermore interactions between the flow structures will tend to happen more often as seen in figure 7(*d*). Figure 21 shows four vortex pairs, $Q1$–$Q4$ at $30.25T$. The flow structures $Q2$ and $Q3$ approach each other and amalgamate into a new vortex pair $Q5$ at $32.25T$. On the left side the pair $Q1$ remains relatively stable throughout the five cycles. The vortex pair $Q4$ on the right side exhibits a distorted shape with detached vorticity regions such as that seen at $32.25T$; the shape of this structure is far from being symmetric in contrast to that observed at lower β. An *et al.* (2011) also discussed the emergence of new vortices

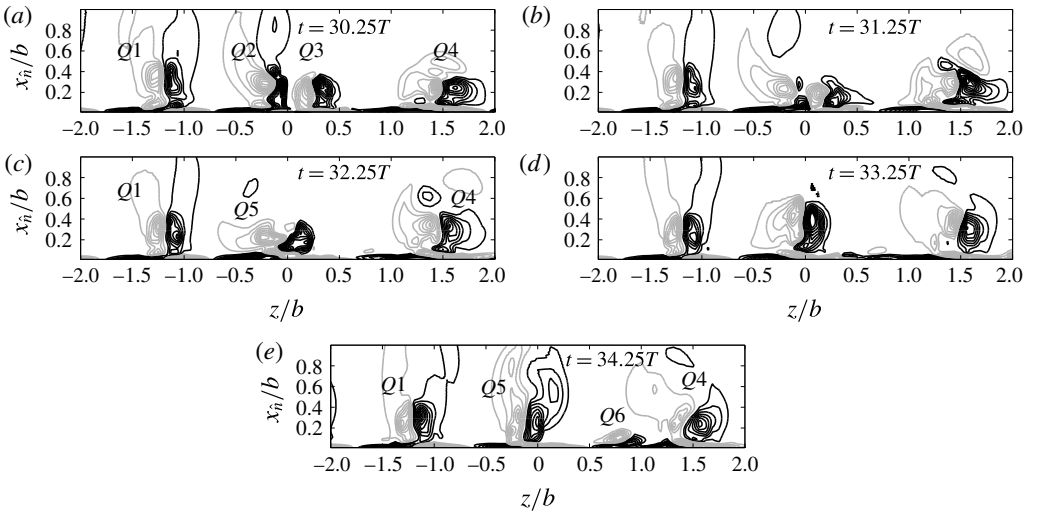

FIGURE 21. As figure 20 but $\beta = 600$.

when the spacing between two vortices is substantially larger than the average spacing between contiguous vortices. This is observed at $34.25T$ between $x/b = 0.5$ and 1.0 in figure 21, where an incipient flow structure labelled as $Q6$ can be observed. By further increasing the frequency parameter β the originally well-organized structure of vortices will eventually break down.

6. Concluding remarks

In this work we have investigated the oscillating flow past elliptic cylinders by directly integrating the three-dimensional Navier–Stokes equations forward in time. Our main objective has been to explore flow regimes corresponding to the early development of three-dimensional instabilities, and to compare our results with a previous instability theory for oscillating flow around elliptic cylinders (Hall 1984). Then, a more in-depth analysis of the flow configuration with highest ellipticity ($\Lambda = 1/3$) has been conducted for a range of frequency parameters β in order to understand the processes of vortex formation.

For the high-eccentricity case $\Lambda = 1/3$ the flow field remained two-dimensional at the lowest Stokes number $\beta = 200$ whereas the originally two-dimensional flow evolved into a three-dimensional flow field for the higher Stokes numbers in table 1. Moreover, the higher the β-values considered, the earlier the departure from strict two-dimensionality and the more irregular the resulting flow field observed, as shown in figure 7. It should be noted, however, that the ratio between the global Taylor number Ta and the critical value of the global Taylor number for a circular cylinder Ta_0 varied from 11.7 for $\beta = 200$ to 20.3 for $\beta = 600$. This implies that the simulated flow field became unstable at a Ta/Ta_0-value about 10 times higher than the stability limit that resulted from Hall's theoretical considerations and reproduced here as the lower branch in figure 1(*a*). One should recall that Hall's linear stability analysis identified the conditions for marginal stability at one specific location and at the particular instant of time that corresponded to maximum flow velocity. It is likely, however, that for a three-dimensional instability to grow, the unstable conditions

have to extend over a finite region in space and over a finite time interval. If so, a significantly higher Taylor number than that predicted by the theory will be required for a minute disturbance of the two-dimensional flow field to evolve in time.

Visualizations of vorticity isosurfaces taken at the same phase for five different aspect ratios of $\Lambda = 1/3,\ 1/2,\ 2/3,\ \sqrt{3/5}$ and 1 have shown that the main flow structure originally identified as 'streaked flow' by Honji (1981) is retained for elliptic cylinders. As expected, the configurations with low eccentricity ($\Lambda = 2/3$ and $\sqrt{3/5}$) exhibited rib-like structures in staggered bands at each side of the cylinder, similar to those previously observed for circular cylinders (see e.g. Honji 1981; Tatsuno & Bearman 1990; An *et al.* 2011; Suthon & Dalton 2012). When the aspect ratio was decreased further to $\Lambda = 1/2$ the vortex pairs experienced a shifting towards the stagnation point, in accordance with the theoretical predictions (Hall 1984). For $\Lambda = 1/3$ the vortical structures were distorted into an oblate shape with an antisymmetric distribution with respect to the (x, z)-plane. An interesting feature for $\Lambda = 1/3$ and $1/2$ was the presence of a pair of counter-rotating spanwise vortex cores that originates near the tip of the ellipse due to increased local curvature for low Λ.

The spatio-temporal evolution of the flow structures was examined in detail for $\Lambda = 1/3$ with fixed $KC = 2.0$ and Stokes number in the range $200 \leqslant \beta \leqslant 600$. The flow at $\beta = 200$ was characterized by the absence of three-dimensional structures; it is worth mentioning that at this (KC, β)-combination a circular cylinder already exhibits Honji vortices. The basic two-dimensional structure for this case was tracked during a half-cycle, revealing Stokes layers with opposite vorticity as previously reported for oscillating flow around circular cylinders. Indeed, the agreement with Stokes' solution for the flow over an oscillating flat plate (Stokes' second problem) is very good up to $0.05b$ from the cylinder wall. We also observed two counter-rotating vortex cores which form near the tip of the ellipse and are convected along the cylinder walls by the ambient flow. These two regions of concentrated vorticity gradually diffuse as they approach the opposite tip of the ellipse, but their strength increases with β.

The basic two-dimensional flow experiences three-dimensional instabilities when the frequency parameter β is increased further to 300 and 400. The flow structures are stable and evenly distributed along the cylinder span, resembling the arrangement observed in oscillatory flows around circular cylinders. Contrary to the circular cylinder case, however, the evolution of the three-dimensional flow structures during one cycle of oscillation shows an initial growth up to $\approx T/4$ followed by decay of circulation as the instability develops near the opposite tip of the ellipse. The four locations at which the three-dimensional instability starts to develop for $\Lambda = 1/3$ are in remarkably good agreement with Hall's theory. The case with $\beta = 400$ experiences a drifting of the flow structures along the span after sufficiently long simulation time. With a further increase of β to 500 and 600 the structures exhibit merging of regions with opposite vorticity as well as generation of new pairs of vortices.

It is finally noteworthy that a complete period T was required to portray the time evolution of the three-dimensional flow structures for an elliptic cylinder, as shown in figures 17 and 18, whereas only a half-period $T/2$ is needed for a circular cylinder; see e.g. figure 13 in An *et al.* (2011). Moreover, while the Honji vortices that occurred on a circular cylinder persisted throughout the entire oscillation period (see figure 12 in An *et al.* 2011), the circulation associated with the vortical structures on the elliptic cylinder was not sustained throughout the period (see figure 19).

Acknowledgements

The authors are grateful to the anonymous referees for their significant and constructive comments. This work has received support from the Research Council of Norway (Program for Supercomputing) through a grant of computing time.

REFERENCES

AN, H., CHENG, L. & ZHAO, M. 2011 Direct numerical simulation of oscillatory flow around a circular cylinder at low Keulegan–Carpenter number. *J. Fluid Mech.* **666**, 77–103.

BADR, H. M. & KOCABIYIK, S. 1997 Symmetrically oscillating viscous flow over an elliptic cylinder. *J. Fluids Struct.* **11**, 745–766.

BEARMAN, P. W., DOWNIE, M. J., GRAHAM, J. M. R. & OBASAJU, E. D. 1985 Forces on cylinders in viscous oscillatory flow at low Keulegan–Carpenter numbers. *J. Fluid Mech.* **154**, 337–356.

ELSTON, J. R., BLACKBURN, H. M. & SHERIDAN, J. 2006 The primary and secondary instabilities of flow generated by an oscillating circular cylinder. *J. Fluid Mech.* **550**, 359–389.

HALL, P. 1984 On the stability of the unsteady boundary layer on a cylinder oscillating transversely in a viscous fluid. *J. Fluid Mech.* **146**, 347–367.

HONJI, H. 1981 Streaked flow around an oscillating circular cylinder. *J. Fluid Mech.* **107**, 509–520.

JEONG, J. & HUSSAIN, F. 1995 On the identification of a vortex. *J. Fluid Mech.* **285**, 69–94.

KEULEGAN, G. H. & CARPENTER, L. H. 1958 Forces on cylinders and plates in an oscillating fluid. *J. Res. Natl Bur. Stand.* **60**, 423–440.

MANHART, M. 2004 A zonal grid algorithm for DNS of turbulent boundary layers. *Comput. Fluids* **33**, 435–461.

MANHART, M., TREMBLAY, F. & FRIEDRICH, R. 2001 MGLET: a parallel code for efficient DNS and LES of complex geometries. In *Parallel Computational Fluid Dynamics-Trends and Applications*, pp. 449–456. Elsevier.

MORISON, J. R., O'BRIEN, M. P., JOHNSON, J. W. & SCHAAF, S. A. 1950 The force exerted by surface waves on piles. *Petrol. Trans. AIME* **189**, 149–157.

PELLER, N., LE DUC, A., TREMBLAY, F. & MANHART, M. 2006 High-order stable interpolations for immersed boundary methods. *Intl J. Numer. Meth. Fluids* **52**, 1175–1193.

SARPKAYA, T. 1986 Force on a circular cylinder in viscous oscillatory flow at low Keulegan–Carpenter numbers. *J. Fluid Mech.* **165**, 61–71.

SARPKAYA, T. 2002 Experiments on the stability of sinusoidal flow over a circular cylinder. *J. Fluid Mech.* **457**, 157–180.

SARPKAYA, T. 2005 On the parameter $\beta = Re/KC = D^2/\nu T$. *J. Fluids Struct.* **21**, 435–440.

SARPKAYA, T. 2006 Structures of separation on a circular cylinder in periodic flow. *J. Fluid Mech.* **567**, 281–297.

STONE, H. L. 1968 Iterative solution of implicit approximations of multidimensional partial differential equations. *SIAM J. Numer. Anal.* **5**, 530–558.

SUTHON, P. & DALTON, C. 2011 Streakline visualization of the structures in the near wake of a circular cylinder in sinusoidally oscillating flow. *J. Fluids Struct.* **27**, 885–902.

SUTHON, P. & DALTON, C. 2012 Observations on the Honji instability. *J. Fluids Struct.* **32**, 27–36.

TATSUNO, M. & BEARMAN, P. W. 1990 A visual study of the flow around an oscillating circular cylinder at low Keulegan–Carpenter numbers and low Stokes numbers. *J. Fluid Mech.* **211**, 157–182.

WHITE, F. M. 2006 *Viscous Fluid Flow*, 3rd edn. McGraw-Hill.

WILLIAMSON, C. H. K. 1985 Sinusoidal flow relative to circular cylinders. *J. Fluid Mech.* **155**, 141–174.

WILLIAMSON, J. H. 1980 Low-storage Runge–Kutta schemes. *J. Comput. Phys.* **56**, 48–56.

YANG, K. 2014 Oscillatory flow past cylinders at low *KC* numbers. PhD thesis, The University of Western Australia.

YANG, K., CHENG, L., AN, H., BASSOM, A. P. & ZHAO, M. 2014 Effects of an axial flow component on the Honji instability. *J. Fluids Struct.* **49**, 614–639.

ZHANG, J. & DALTON, C. 1999 The onset of three-dimensionality in an oscillating flow past a fixed circular cylinder. *Intl J. Numer. Meth. Fluids* **42**, 19–42.